A First-Principles Study of the Atomic Structures and Catalytic Properties of Monolayer TaS_2 with Intrinsic Defects

Nan Gao[a], Xiaoqing Liang[a], Jijun Zhao[b], Yue Chen[c,*]

[a] *School of Electronics and Information Engineering, Taizhou University, Taizhou, 318000, China*

[b] *Key Laboratory of Materials Modification by Laser, Ion and Electron Beams (Dalian University of Technology), Ministry of Education, Dalian 116024, China*

[c] *Department of Mechanical Engineering, The University of Hong Kong, Pokfulam Road, Hong Kong SAR, China*

Abstract

Monolayer tantalum disulfide (TaS_2) has attracted much attention for its superconducting and charge-density-wave (CDW) properties. However, multiple structural defects are frequently observed in fabricated samples and greatly influence their performance. Using first-principles calculations, we systematically investigate the atomic structures, energetic stability, electronic and catalytic properties of six common point defects and six grain boundaries (GBs) of monolayer TaS_2. The single S atom vacancy defect of monolayer TaS_2 has the lowest formation energy below 2 eV, regardless of the chemical environment. For GBs, 4|4 and 4|8 defect rings without homoelemental bonds are predicted to form more easily than the 5|7 defect ring. For the hydrogen evolution reaction (HER) process, the binding strengths of different defect sites are related to the *p* or *d* band center of the S or Ta atom, respectively. In particular, TaS_2 with a single S vacancy defect shows superior catalytic activity with a H atom adsorption energy of 0.1 eV and a Tafel barrier of 0.25 eV. These theoretical results provide vital guidance for detecting various defects of two-dimensional TaS_2 in experiments and modulating catalytic properties via defect engineering.

Keywords: TaS_2, grain boundary, binding strength, hydrogen evolution reaction

---

[*] Corresponding author. Email: yuechen@hku.hk (Y. Chen).

1. INTRODUCTION

Two-dimensional (2D) transition metal dichalcogenides (TMDs) have attracted great interest for their unique electronic, optical and chemical properties in an extensive range of promising applications.[1-4] The traditional TMD monolayer MoS_2, a semiconductor with a direct band gap of 1.8 eV,[5] has been widely fabricated for field-effect transistors, photoelectric detectors, solar batteries and so on.[6-10] Recently, VB subgroup TMDs composed of 2D TaS_2 and NbS_2 have gradually entered researchers' field of view due to their extraordinary superconductivity compared to other common 2D materials.[11-16] The existence of defects including the change in stacking order and the intrinsic defect induced disorder in TaS_2 nanosheets can effectively enhance the superconducting critical transition temperature (T_c) by approximately 3 K.[17-18] On the other hand, topological defects in TaS_2 can effectively modulate the phonon dynamics,[19] charge density wave states,[20] periodic lattice distortions,[21] and electrocatalytic activities.[22]

Substantial point and line defects have been detected in TaS_2 in experiments. Kingyanjui et al. found plentiful S vacancies caused by high-energy electron irradiation[21] and demonstrated that increased S vacancies with lower formation energy can lead to dislocations according to their DFT calculations. Additionally, nonhexagon polygons including 5|7 disclination pairs, and quadrangle and octagon defect rings were observed using high-resolution transmission electron microscopy (HRTEM). In scanning tunneling microscopy (STM) measurements, Se substitution defects with different doping concentrations were detected in TaS_2, and a transition from the Mott insulating state to the metallic state was reported.[23] Peng et al. revealed that Ta atom defects modulated by acidic conditions enhanced the carrier density and electron-phonon interaction, contributing to the superconducting performance.[17]

2D TMDs, such as MoS_2 and WS_2, with large surface areas and active edge defect sites, are regarded as promising electrocatalysis materials for HER evolution.[24-27] However, the semiconductor character limits the electrical conductivity and catalytic activity. Inducing large lattice bending and realizing a high concentration of 1T phase MoS_2 were demonstrated as effective methods for decreasing the Tafel slope of 1T

MoS_2 to 40 mV/dev and further improving its catalytic activity.[28-29] Similarly, TaS_2 thin films possess an intrinsic metallic character and have been demonstrated as high-efficiency catalysts in electrochemical reactions.[30-34] For instance, Liu et al. revealed that the current density can reach 10 mA cm^{-2} with an overpotential of approximately 50~60 mV at the highly active basal-plane sites of TaS_2,[30] exceeding the performance of previously reported TMDs. Uniform thickness and domain size ensure superior dispersibility in ethanol and promote the reaction efficiency of the HER.[32-33] In addition, novel vertically oriented TaS_2 fabricated via substrate engineering regulation possesses an ultrahigh exchange current density of approximately 67 μA cm^{-2} and a relatively low Tafel slope of 67-82 mV dec^{-1}.[34]

Despite the progress discussed above, a few issues are yet to be resolved. What are the morphologies of different point and line defects of monolayer TaS_2 detected in experiments? What are the relative dynamic stabilities of these defects in different chemical potential environments? Considering the outstanding metallic properties of 2D TaS_2, how do the different defect sites influence its catalytic activity? To answer these questions, here, we systemically investigate the structure, stability, electronic and catalytic properties of a series of point and line defects in monolayer TaS_2 via DFT calculations. A single S vacancy defect is found to form easily regardless of the chemical environment. The energy barrier for forming H_2 is as low as 0.25 eV in the HER process. H atom adsorbing on the Ta site is found to be more stable than that on the S site in both point and line defect configurations. These theoretical results pave the way to experimentally identifying the intrinsic defects in TaS_2 nanosheets, and to making use of these defects to achieve an improved performance in electrocatalytic applications.

2. COMPUTATIONAL METHODS

Spin-polarized density functional theory (DFT)[35] calculations were carried out using the Vienna ab initio simulation package (VASP).[36] The planewave basis set with an energy cutoff of 450 eV, the projector augmented wave (PAW) potentials,[37-38] and the generalized gradient approximation (GGA) parameterized by Perdew, Burke and

Ernzerhof (PBE) for the exchange-correlation functional[39] were applied. DFT-D3 dispersion correction method was adopted to better describe the van der Waals (vdW) interaction.[40] To avoid interaction between neighboring regions, we used rectangular 5 × 5 supercells of monolayer TaS_2 to describe different point defects, and a large lateral distance of 18 Å between a GB and its replica. A vacuum region of 18 Å was added in the vertical direction to eliminate interaction between neighboring layers. The Brillouin zone of the supercell was sampled by a uniform **k**-point mesh with a spacing of $2\Pi \times 0.03$ Å^{-1}. The model structures were fully optimized for both cell dimensions and ionic degrees of freedom with thresholds of 10^{-6} eV for the total energy and of 0.02 eV/Å for the forces on each atom. The kinetic process of the HER including the energy barrier and transition state was studied using the climbing-image nudged elastic band (CI-NEB) method implemented in VASP.[41] Transmission electron microscopy (TEM) images of different point defects and GBs were simulated using QSTEM software.[42] The experimental in-plane and out-of-plane lattice parameters of bulk TaS_2 are 3.36 Å and 5.90 Å, respectively,[43] which are well accorded with our calculated results of $a = b = 3.34$ Å and $c = 5.87$ Å.

3. RESULTS AND DISCUSSION

3.1. Structures and formation energies of TaS_2 point defects and GBs

We consider six typical point defects frequently observed in experiments, including the monosulfur vacancy (V_S), two sulfur vacancy (V_{S2}), TaS_6 vacancy (V_{TaS6}), TaS_3 vacancy (V_{TaS3}), and antisite defects where two S atoms substitute a Ta atom ($S2_{Ta}$) and a Ta atom substitutes two S atoms (Ta_{S2}). As shown in Figure 1a, TaS_2 containing different vacancies or antisite defects show a planar structure, while those atoms near the defect sites have relatively large displacements compared to pristine TaS_2. (The detailed bond lengths and angles around defect sites for all optimized structures are shown in Figure S1 of the supporting information). The Ta-S bond length around a point defect is 2.38-2.54 Å, close to that in pristine TaS_2 (2.48 Å). Antisite defects can induce S-S and Ta-Ta homoelemental bonds (bond lengths of approximatelly 2.20 and 2.45 Å, larger than those in MoS_2 of 2.11 and 2.31 Å).[44] To better understand the common point defects observed in experiments, we simulated TEM images based on our relaxed structures, as shown in the bottom panels in Figure 1a. Overall, the Ta atoms with a larger atomic mass in the middle of the sandwich configuration have a higher partial charge density (shown in red) than the S atoms at both ends (shown in yellow) of TaS_2. The single S atom projection has a lower charge density (shown in green) for V_S and V_{TaS3} defects. For $S2_{Ta}$ and Ta_{S2} antisite defects, substituted S and Ta atoms in TEM images have almost identical brightness to those in pristine TaS_2.

To characterize the energetic stability of these point defects, the formation energy is calculated as:

$$E_f = E_{tot} - \sum_i N_i \mu_i - E_{per} \tag{1}$$

where E_{tot} is the total energy of a point defect, E_{per} is the energy of the corresponding perfect TaS_2 supercell, μ_i is the chemical potential, and N_i is the number of excess or deficient atoms. Figure 1b shows the formation energies of different point defects as a function of sulfur chemical potential. The positive/negative slopes of different systems are proportional to the numbers of deficient/excess sulfur atoms labeled by orange/green lines. At equilibrium, the chemical potentials of S and Ta satisfy the relation $2\mu_S + \mu_{Ta} = \mu_{TaS2}$, where μ_{TaS2} is the chemical potential of a unit cell of TaS_2. The left boundary corresponds to the Ta-rich condition, where the chemical potential of S is calculated as $\mu_S = (\mu_{TaS2} - \mu_{Ta})/2 = -5.69$ eV; μ_{TaS2} and μ_{Ta} represent the total energies of a formula unit of TaS_2 and one Ta atom in its cubic phase, respectively. The right boundary corresponds to the S-rich condition, where the S chemical potential is taken as the total energy of one S atom in its orthorhombic phase, and it is equal to −4.09 eV. It is seen that the V_S vacancy generally has the lowest formation energy below 2 eV regardless of the S chemical potential environment, consistent with a previous study of MoS_2.[45] The formation energies of V_{S2} and V_{TaS3} under Ta-rich conditions are below 2 eV, whereas $S2_{Ta}$ and V_{TaS3} under S-rich conditions with formation energies below 3 eV, can form more easily than other defects. Larger vacancy defects in other common TMDCs ($MoSe_2$, $MoTe_2$, WS_2, WSe_2 and WTe_2) were reported to have formation energies in a range from 2.81 to 3.38 eV,[46-48] which are generally larger than that in TaS_2. V_{TaS3} has a much lower formation energy than

V_{TaS6}, which may be attributed to the similar S vacancy chemical environments for V_{TaS3} and V_S, as can be seen from the TEM images. Simulated TEM images show that the loss of surface sulfur atoms in V_{TaS3} and V_S defects causes lower brightness around S, comparing to that in pristine TaS_2. In terms of chemical potential, both V_{TaS3} and V_S defects have a deficiency of one sulfur atom, resulting in an identical slope in the relationship between formation energy and sulfur chemical potential, as shown in Figure 1b. On the other hand, antisite defect $S2_{Ta}$ under S rich conditions is predicted to form more easily than Ta_{S2} under Ta rich conditions, which can be understood by the decrease in the homoelemental bond length from 2.45 Å (Ta-Ta bond in TaS_2) to 2.20 Å (S-S bond in $S2_{Ta}$), hence improving the structural stability. In comparison, Ta_{S2} and V_{TaS6} with higher formation energies may not be observed in experiments except for under extreme irradiation damage conditions.

In addition to point defects, different types of grain boundaries (GBs) are often observed in TMD sheets.[49-52] Based on the commonly observed GBs, we construct six TaS_2 GBs including 4|4 defect rings for (1,1)|(1,1) and (1,1)|(1,1)i2, 5|7 defect rings for (2,2)|(3,1) and (3,1)|(3,1), and 4|8 defect rings for (3,0)|(3,0) and (1,1)|(1,1)i3, as shown in Figure 2a. Different GBs are designated by translation vectors (n_L, m_L) and (n_R, m_R) at the left and right domains of the GB. For those GBs with the same translation vectors, we use $(n_L, m_L)|(n_R, m_R)\mathrm{i}N$ to distinguish them. To better characterize the energetic stability of GBs, the formation energy is defined as

$$E_f' = (E_{GB} - N_{uc}E_{uc})/2L \quad (2)$$

where E_{GB} is the total energy of the TaS_2 GB; N_{uc} and E_{uc} correspond to the number and energy of the TaS_2 unit cell, respectively; L is the periodic length; and the factor 2 represents the GB and its replica in the computational model. The structural parameters and energetic information are summarized in Figure 2b and Table S1. The formation energies of TaS_2 GBs are generally within the range of 0.18-0.41 eV/Å, much lower than those of MoS_2 GBs (0.34-1.00 eV/Å)[44] and higher than those of phosphorene GBs (0.09−0.24 eV/Å).[53] In contrast, 5|7 defect rings including (2,2)|(3,1) and (3,1)|(3,1) GBs, have a relatively high E_f' of approximately 0.4 eV/Å due to the unsaturated Ta and S atoms, consistent with a previous investigation on MoS_2 GBs.[44]

Moreover, simulated TEM images are shown below the corresponding GB models, where green, orange, and red represent the charge density projections of a single S atom, two S atoms, and a single Ta atom, respectively.

3.2. Electronic and catalytic properties of pristine TaS_2

To examine the catalytic properties of monolayer TaS_2, we first analyze the features of Ta-S bonds based on the electron localization function (ELF). The ELF is usually viewed as a contour plot in real space and its values vary from 0 to 1. An ELF value of approximately 1 denotes perfect localization of electrons, 0 respresents low electron density, and 0.5 indicates a free electron gas.[54] The ELF of TaS_2 on the (001) and (110) planes is presented in Figure 3a. For the (001) plane, the ELF slice is cut along the middle of the Ta-S bond. Evidently, electrons localize mainly around the projected S atoms (yellow spheres) and the ELF is approximately 0.4-0.7 between Ta and S atoms, indicating the formation of chemical bonds. The bottom panel shows the ELF distribution on the (110) plane. The ELF value approaches 0.5 around the Ta-S chemical bonds, suggesting that electrons can transport freely to some extent. Such results can also be demonstrated from Bader charge analysis. Each S atom in TaS_2 gains approximately 0.76 electrons on average which is more than that in MoS_2 (0.49), suggesting stronger ionic bonding between Ta and S atoms.

To further investigate the electronic properties of monolayer TaS_2, we calculate the projected electronic band structure of Ta/Mo and S elements, as shown in Figure 3b and Figure S2 in the Supporting Information. Monolayer MoS_2, as a two-dimensional semiconductor, has a band gap of 1.67 eV at the high-symmetry K point, in accordance with previous PBE calculations.[55] The valence band maximum (VBM) is mainly contributed by $d_{x^2-y^2}$ orbitals at K point (dark blue) and d_{z^2} orbitals at the Γ point (purple) of Mo atoms. The conduction band minimum (CBM) is mainly constituted by d_{z^2} orbitals at the K point (purple) of Mo atoms, whereas S atomic orbitals have almost no contribution to the VBM and CBM. Different from monolayer MoS_2, the band structure of TaS_2 is shifted by approximately 0.57 eV, leading to crossing of the Fermi level with the $d_{x^2-y^2}$ and d_{z^2} orbitals of Ta atoms, and a metallic character. Such results are consistent with the above ELF and Bader analyses.

The outstanding electronic properties of monolayer TaS_2 facilitate its potential application in electrocatalysts for the hydrogen evolution reaction (HER).[30-33] Generally, the HER in acidic media involves two reaction steps: (1) electrochemical hydrogen adsorption: $H^+ + e^- \rightarrow H^*$ (Volmer reaction) and (2) electrochemical desorption: $H^* + H^+ + e^- \rightarrow H_2$ (Heyrovsky reaction) or $H^* + H^* \rightarrow H_2$ (Tafel reaction). First, we examine the Volmer reaction process by calculating the partial density of states (PDOS) before and after H atom adsorption, as shown in Figure 3c. The 1*s* orbital of an isolated H atom is half occupied at the Fermi level and it overlaps with the three projected 3*p* orbitals of the S atoms before the H atom is adsorbed. When H is adsorbed on the top site of S atom, the 1*s* orbital of the H atom is shifted to deeper valence bands around -7.2 eV, well matching with the $3p_z$ of the S atom, leading to the formation of bonding states (σ) between H* and TaS_2 in Figure 3d. Meanwhile, the conduction bands at approximately 2.8 eV induce antibonding states (σ*). As a reference, the PDOS of a single H atom adsorbed on MoS_2 is shown in Figure S3 in the Supporting Information. On the one hand, the electronic 1*s* states of an isolated H atom still exist in the vicinity of the Fermi level after adsorption, meaning that the binding H* strength is lower in MoS_2 than in TaS_2. On the other hand, there is no strong orbital hybridization among the three 3*p* orbitals of S atoms and H atom orbitals in the deeper valence bands as in TaS_2. These results reveal that the superior conductivity and stronger coupling between the H atom and monolayer TaS_2 may effectively improve the catalytic performance of TaS_2 in the HER.

3.4. Catalytic properties of TaS_2 point defects and GBs

A number of investigations have demonstrated that edge and basal plane defects in MoS_2 nanosheets benefit the electrocatalytic HER performance. Herein, we systematically explore the catalytic properties of four easily formed point defects and six representative GBs of monolayer TaS_2 as discussed above. For the Volmer reaction, the free energy of formation for hydrogen adsorption (ΔG_{H^*})[56] reflects the catalytic activity of the HER and is defined as:

$$\Delta G_{\mathrm{H}^*} = \Delta E_{\mathrm{H}^*} + \Delta \mathrm{ZPE} - T\Delta S \qquad (3)$$

where ΔE_{H^*}, ΔZPE and ΔS are the H* binding energy, zero-point energy and entropy differences between the adsorbed H* and gaseous H_2 phase. The temperature (T) is set as 298.15 K in this work and the values of ΔZPE and ΔS can be obtained from the NIST-JANAF thermodynamics table.[57] $\Delta G_{\mathrm{H}^*} = 0$ corresponds to an ideal HER catalyst, and a positive (negative) ΔG_{H^*} value indicates a weak (strong) interaction between H* and the catalyst, which is beneficial for H* desorption (adsorption). As shown in Figure 4a, S4 and Table S1, for point defects that have relatively low $\Delta G_{\mathrm{H}^*} <$ 0.2 eV, H atom can stably adsorb at the top site of S atom, except for V_{S2} system where the H atom is bonded with three surrounding Ta atoms, resulting in a decrease in ΔG_{H^*} to -0.74 eV. For 4|4 defect ring (1,1)|(1,1) and (1,1)|(1,1)i2 GBs, the top S atom is the stable adsorption site for the H atom and they have relatively high ΔG_{H^*} values of 0.34 eV and 0.47 eV, respectively. For other GBs including 5|7 rings and 4|8 rings, the H atom prefers to bond with two neighboring Ta atoms as shown in Figure S5 in the Supporting Information, and ΔG_{H^*} decreases to 0.05 ~ -0.34 eV, benefiting the adsorption of the H atom. On the other hand, Bader charge analysis shows that the formation of defect can enhance the charge transfer between H and monolayer TaS_2 compared to the pristine system (see Figure S6 of supporting information). To gain further insight into the HER activity of different types of TaS_2 defects, the PDOS of S and Ta atoms is plotted in Figure 4b and 4c, respectively. Among these defects, the profiles of valence band states are almost the same (highlighted by gray regions) and the differences in the PDOS caused by intrinsic defects are mainly related to the conduction states from 1 to 3 eV. For the top S adsorption sites, the 3*p* orbitals of the S atoms are mainly distributed in the valence band regions, and the *p* band center ranges from -3.25 eV to -2.99 eV. Different from the S adsorption sites, when the H atom is adsorbed by two or three Ta atoms, the *d* orbitals of the Ta atoms have partial contributions to the conduction bands, and the *d* band center is located at a deeper energy level between -3.35 eV and -3.23 eV. All defect systems exhibit metallic behavior, with prominent *d* orbital states of Ta atoms in the vicinity of the Fermi level, indicating their primary contributions to the H* binding and HER catalytic activity.

The relationship between the *d* band center (ε_d) of transition metal Ta or the *p* band center (ε_p) of S and free energy ΔG_{H^*} is shown in Figure 4d. The ε_d of Ta in defect systems is defined as:

$$\varepsilon_d(\varepsilon_p) = \frac{\int_{-\infty}^{0} ED(E)dE}{\int_{-\infty}^{0} D(E)dE} \tag{4}$$

where E corresponds to the energy, and $D(E)$ is the PDOS of Ta *d* orbitals or S *p* orbitals. The ε_d or ε_p band center shows a linear relationship with the lowest ΔG_{H^*} for different defect systems, which well accords with the trend in *d*-band center theory with H* binding for transition metals.[58] Therefore, an appropriate *d* band center can be regarded as a criterion to ensure moderate adsorption strength and catalytic activity for the HER.

To better characterize the catalytic activity of monolayer TaS_2 and its defects, kinetic processes of Tafel reactions including H atom recombination and H_2 release are further studied, as shown in Figure 5. Here, we compare the minimum energy paths and the transition states of two representative defects V_S and the (1,1)|(1,1)i3 GB with relatively low formation energy and ΔG_{H^*} with those of pristine TaS_2. For pristine TaS_2, two H atoms initially adsorb at neighboring S atoms and gradually move close to each other in the desorption process with an energy barrier of 1.36 eV. However, in the V_S defect system, two H atoms tend to adsorb on the same S atom bonded with three Ta atoms and the reaction barrier of breaking H-S bonds decreases to 0.25 eV, which is much lower than the value of 1.32 eV in MoS_2.[59] On the other hand, the most stable configuration in (1,1)|(1,1)i3 GB is H atoms bonded with two Ta atoms in the octagon defect rings; the energy barrier is equal to 1.48 eV, which is close to the value of the pristine system. Hence, the introduction of specific intrinsic defects into monolayer TaS_2 may effectively provide active sites for H* desorption and H_2 formation, further improving the HER catalysis performance via the kinetic process.

4. CONCLUSION

In summary, we systematically explored the structures, stabilities, electronic and catalytic properties of different point defects and grain boundaries in monolayer TaS_2 via first-principles calculations. Homoelemental bonds deteriorate the energetic stability of Ta_{S2} and $S2_{Ta}$ point defects and 5|7 defect rings constituting GBs. The conducting property of monolayer TaS_2 is mainly contributed by the $5d_{z^2}$ and $5d_{x^2-y^2}$ orbitals of Ta atoms. The V_S, V_{TaS3}, and $S2_{Ta}$ point defects, and (3,0)|(3,0) and (1,1)|(1,1)i3 GBs with adsorption free energies in the range from 0.07 eV to 0.21 eV have appropriate catalytic sites for the HER. For different H atom adsorption sites, the free binding energy has an appropriate linear relationship with the *p*/*d* band center of the S/Ta element. In particular, the V_S vacancy defect has a relatively low Tafel barrier of 0.25 eV when two adjacent H atoms form H_2. Our results provide a theoretical guideline to identify the possible point and line defects of monolayer TaS_2 and pave the way to tailoring the electronic and catalytic properties via defect engineering.

Supporting Information

Free energy (ΔG_{H*}) of different point defects and GBs in the TaS_2 monolayer (Table S1), bond length and angles, electronic band structures, partial density of states (PDOS) before and after H atom adsorption, stable structures of point defects and GBs with H atom adsorption and Bader charge analysis (Figure S1, S2, S3, S4, S5 and S6). (PDF)

ACKNOWLEDGMENTS

This work is supported by the National Natural Science Foundation of China (12004272 and 11904251). YC is grateful for the support of the HKU Seed Fund for Basic Research (201811159102 and 201910159090), and the research computing facilities offered by ITS, HKU.

Table 1. Periodic length of GBs (L), number of unit cells in the supercell, misorientation angle (θ), and formation energy (E_f') of different types of TaS_2 GBs.

Type	GB	L (Å)	N_{uc}	θ (deg)	E_f' (eV/ Å)
4|4	(1,1)|(1,1)	3.33	10	0	0.18
	(1,1)|(1,1)i2	3.28	11	0	0.40
5|7	(2,2)|(3,1)	11.82	62	16.1	0.37
	(3,1)|(3,1)	12.03	56	32.2	0.41
4|8	(1,1)|(1,1)i3	5.80	28	0	0.22
	(3,0)|(3,0)	9.89	32	0	0.40

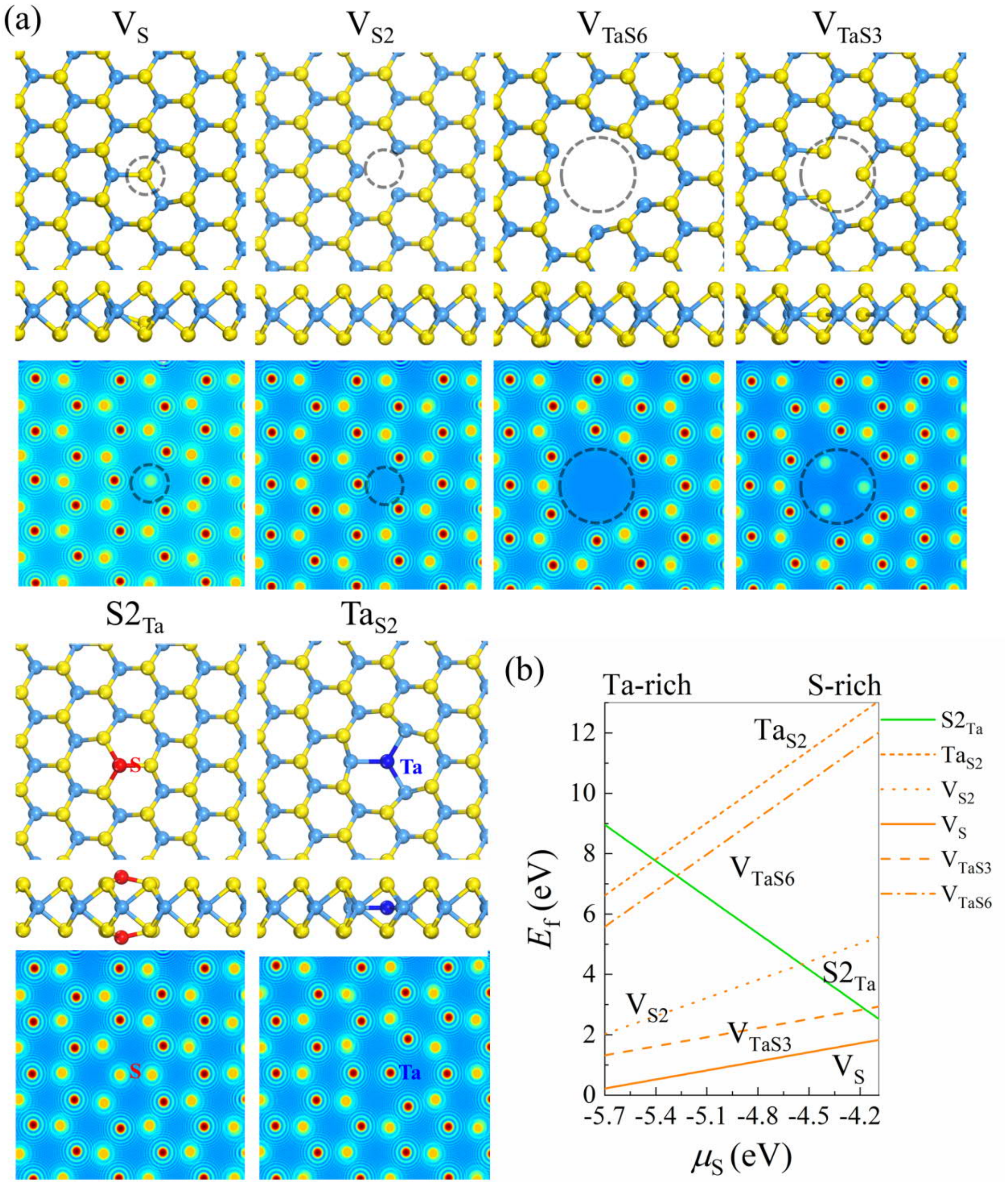

Figure 1. (a) Upper panels: top and side views of atomic structural models of six different point defects, including the monosulfur vacancy (V_S), two-sulfur vacancy (V_{S2}), TaS_6 vacancy (V_{TaS6}), TaS_3 vacancy (V_{TaS3}), two S atoms substituting a Ta atom ($S2_{Ta}$), and a Ta atom substituting two S atoms (Ta_{S2}). The S and Ta atoms are shown in yellow and light blue, respectively; S (Ta) atoms that replace Ta (S) atoms are highlighted in red (blue). The black dashed circles represent the missing S or Ta atoms. Lower panels: simulated transmission electron microscopy (TEM) images based on the corresponding atomic structures. (b) Formation energies of the six different point defects as a function of sulfur chemical potential in the range of -5.69 eV $< \mu_S <$ -4.09 eV.

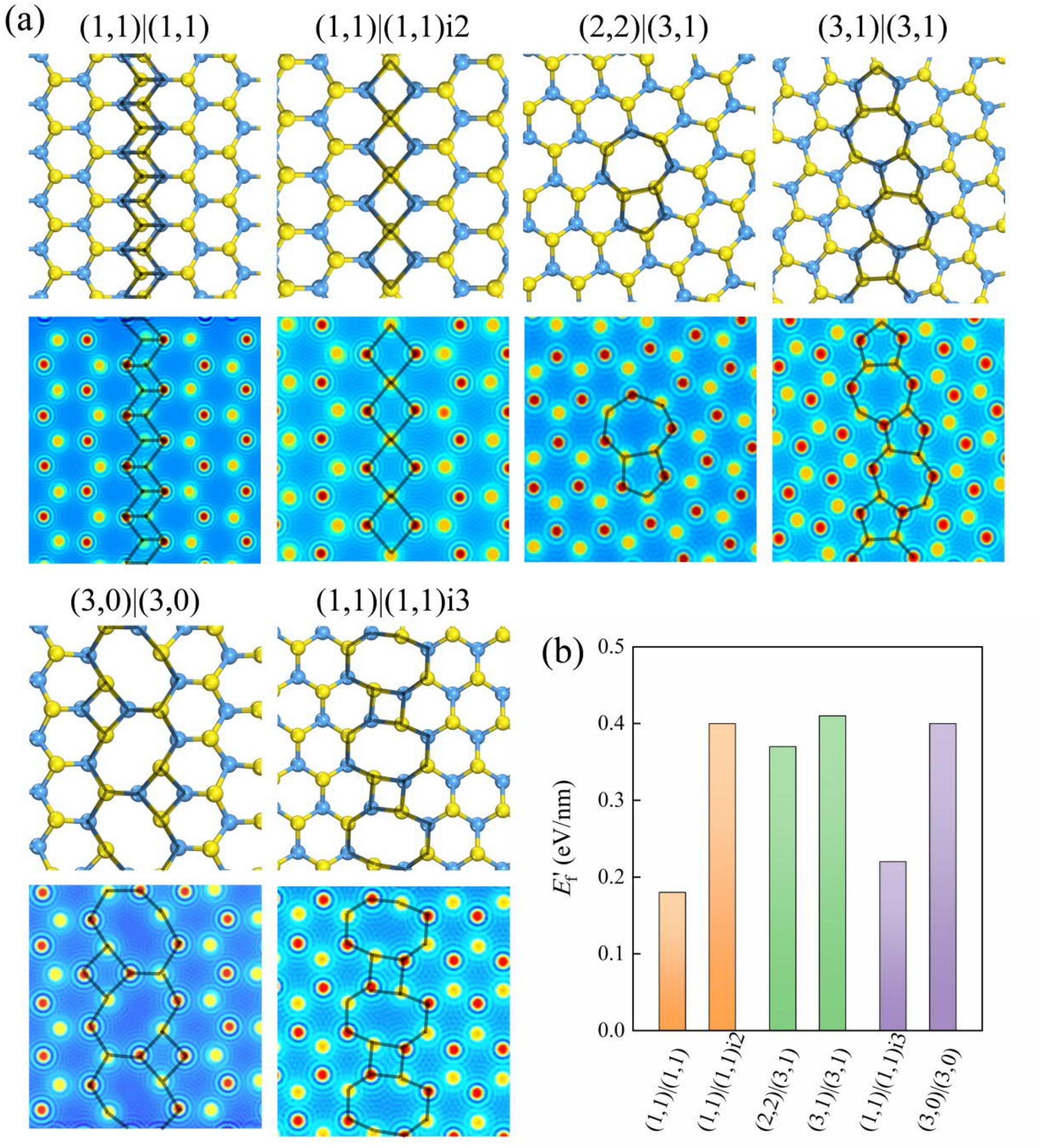

Figure 2. (a) Upper panels: top view of atomic structural models of six different grain boundaries, including 4|4 rings of (1,1)|(1,1) and (1,1)|(1,1)i2, 5|7 rings of (2,2)|(3,1) and (3,1)|(3,1), and 4|8 rings of (3,0)|(3,0) and (1,1)|(1,1)i3. The S and Ta atoms are shown in yellow and light blue, respectively. Lower panels: simulated TEM images based on the corresponding atomic structures. The defect rings are highlighted by black solid lines. (b) Formation energies of the six GBs. The orange, green and purple columns represent the 4|4, 5|7 and 4|8 ring pairs, respectively.

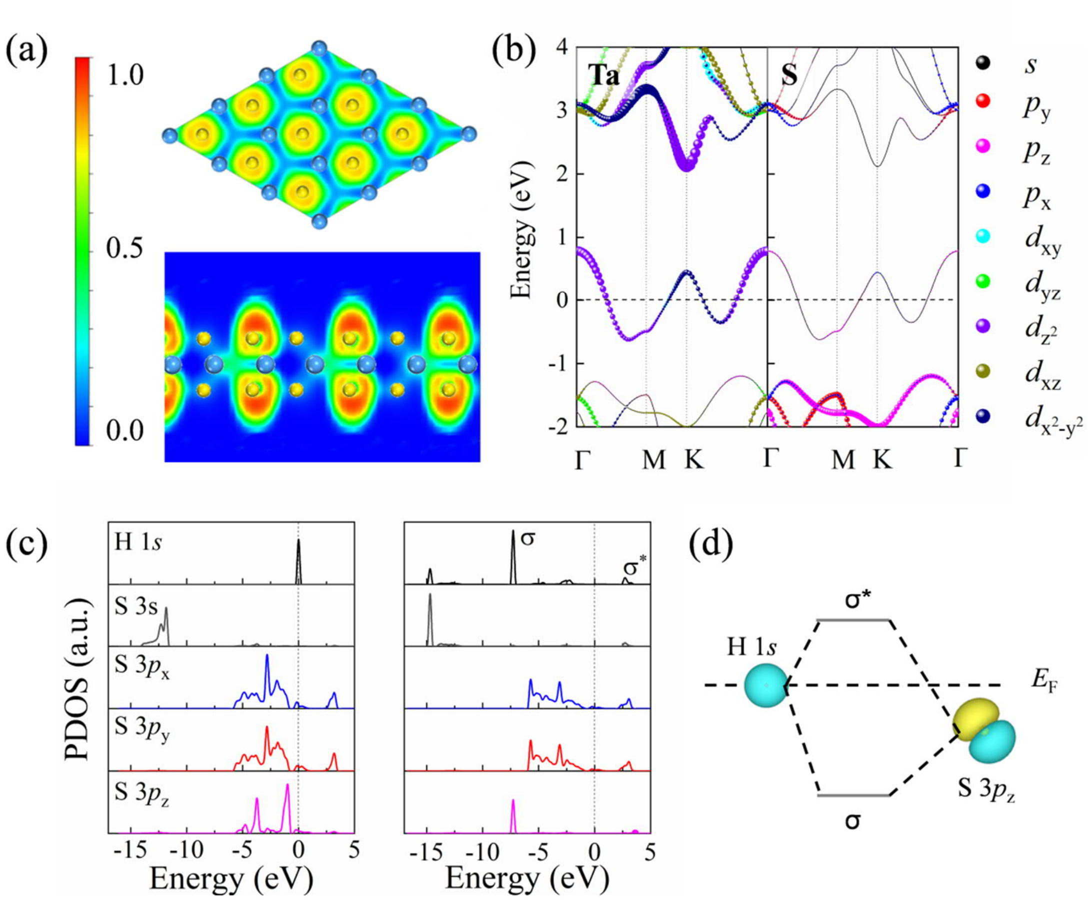

Figure 3. (a) Electron localization functions of monolayer TaS_2 on the (001) and (110) planes. (b) Electronic band structure of monolayer TaS_2 projected onto the Ta and S atoms. Different colors indicate different orbital contributions and the weights are represented by the line widths. The Fermi level is set to zero. (c) Partial density of states (PDOS) of the adsorbed H atom and the nearest surface S atom of monolayer TaS_2 before (left panel) and after (right panel) H atom adsorption. (d) Schematic diagram of the formation of the H-S bond for pristine TaS_2. σ and σ* represent the bonding and antibonding orbitals, respectively.

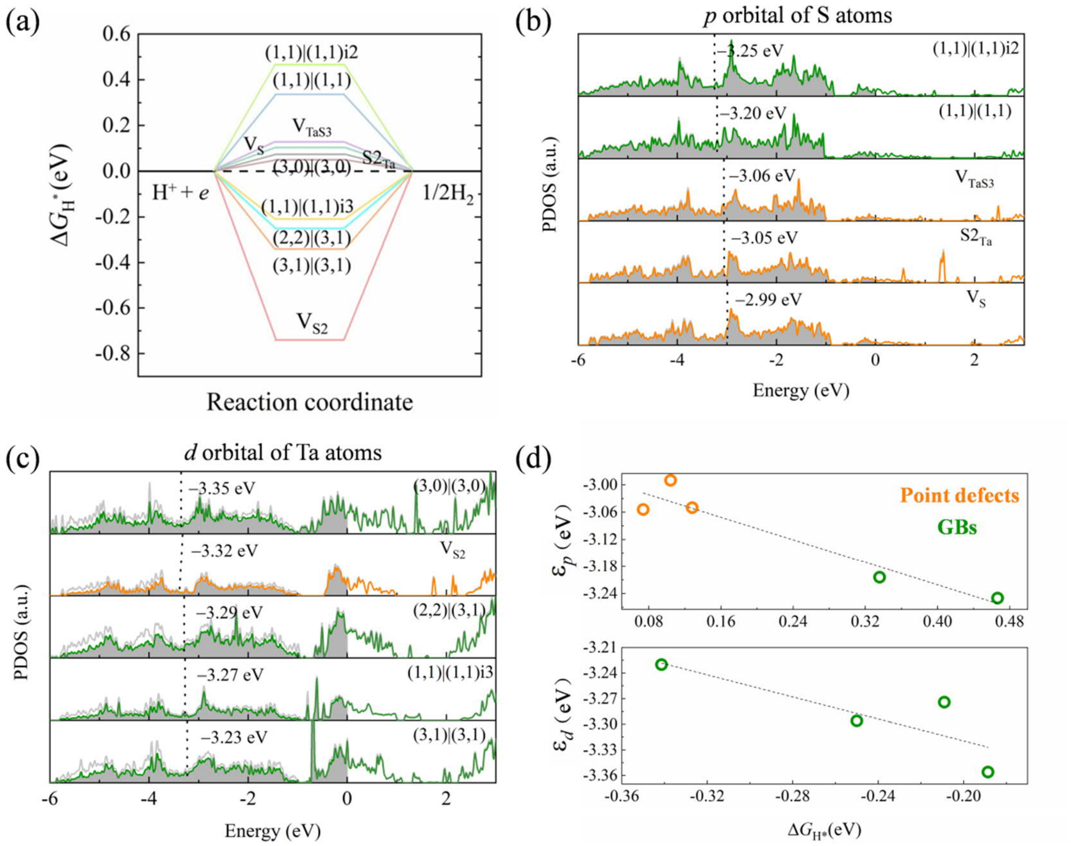

Figure 4. (a) Free energy diagrams for hydrogen evolution at zero potential and pH = 0 on different point defects and GBs of TaS_2. The black dashed line indicates the ideal ΔG_{H*} for HER catalysis. PDOS of the (b) *p* orbitals of the S element and (c) *d* orbitals of the Ta element. The black dashed lines and the values indicate the *p* band centers of S atoms or the *d* band centers of Ta atoms for different defect systems. The Fermi level is set to zero. Occupied states are shown as the gray regions. (d) *p*/*d* band center ($\varepsilon_p/\varepsilon_d$) of the S/Ta element as a function of ΔG_{H*}. The dashed lines are linear fittings.

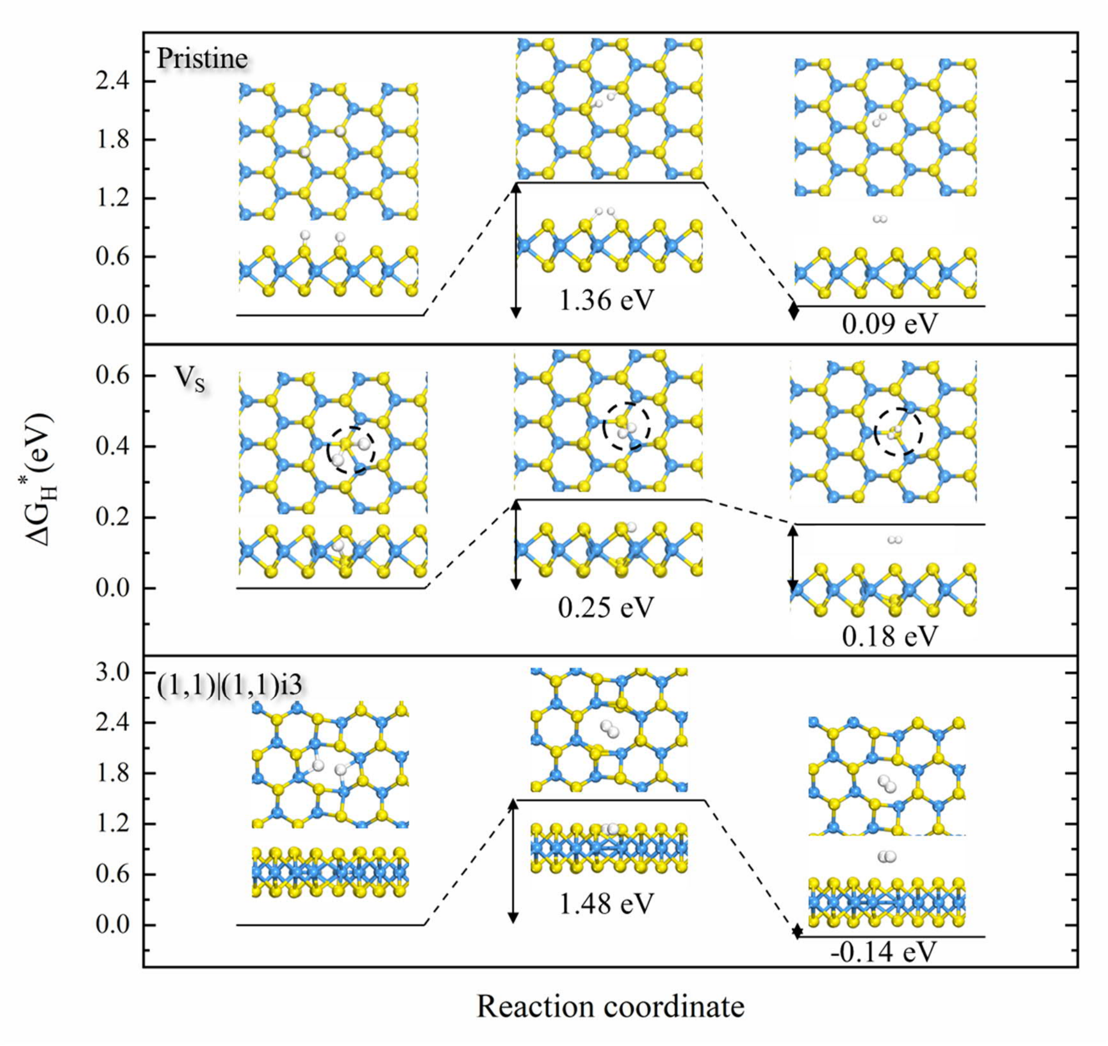

Figure 5. Free energy diagrams of the Tafel reaction for H_2 formation on pristine TaS_2, TaS_2 with a single S vacancy, and TaS_2 with a (1,1)|(1,1)i3 GB. Top and side views of the initial, transition and final states are shown from left to right. The values below the structures indicate the kinetic energy barriers compared to the initial states. H, S and Ta atoms are shown in white, yellow and blue, respectively.

REFERENCES

(1) Choudhary, N.; Islam, M. A.; Kim, J. H.; Ko, T.-J.; Schropp, A.; Hurtado, L.; Weitzman, D.; Zhai, L.; Jung, Y., Two-Dimensional Transition Metal Dichalcogenide Hybrid Materials for Energy Applications. *Nano Today* **2018**, *19*, 16-40.

(2) Zhu, C.; Gao, D.; Ding, J.; Chao, D.; Wang, J., TMD-Based Highly Efficient Electrocatalysts Developed by Combined Computational and Experimental Approaches. *Chem. Soc. Rev* **2018**, *47*, 4332-4356.

(3) Zhang, X.; Lai, Z.; Tan, C.; Zhang, H., Solution-Processed Two-Dimensional MoS_2 Nanosheets: Preparation, Hybridization, and Applications. *Angew. Chem. Int. Ed.* **2016**, *55*, 8816-8838.

(4) Gong, C.; Zhang, Y.; Chen, W.; Chu, J.; Lei, T.; Pu, J.; Dai, L.; Wu, C.; Cheng, Y.; Zhai, T.; et al., Electronic and Optoelectronic Applications Based on 2D Novel Anisotropic Transition Metal Dichalcogenides. *Adv. Sci.* **2017**, *4*, 1700231.

(5) Kin Fai, M.; Changgu, L.; James, H.; Jie, S.; Tony F., H., Atomically Thin MoS_2: A New Direct-Gap Semiconductor. *Phys. Rev. Lett.* **2010**, *105*, 136805.

(6) Kyungjune, C.; Jinsu, P.; Jae-Keun, K.; Keehoon, K.; Tae-Young, J.; Jiwon, S.; Barbara Yuri, C.; Seungjun, C.; Takhee, L., Contact-Engineered Electrical Properties of MoS_2 Field-Effect Transistors Via Selectively Deposited Thiol-Molecules. *Adv. Mater.* **2018**, *30*, 1705540.

(7) Radisavljevic, B.; Radenovic, A.; Brivio, J.; Giacometti, V.; Kis, A., Single-Layer MoS_2 Transistors. *Nat. Nanotechnol.* **2011**, *6*, 147-150.

(8) Kufer, D.; Konstantatos, G., Highly Sensitive, Encapsulated MoS_2 Photodetector with Gate Controllable Gain and Speed. *Nano Lett.* **2015**, *15*, 7307-7313.

(9) Theerthagiri, J.; Senthil, R. A.; Kumar, B. S.; Reddy Polu, A.; Madhavan, J.; Ashokkumar, M., Recent Advances in MoS_2 Nanostructured Materials for Energy and Environmental Applications – a Review. *J. Solid State Chem.* **2017**, *252*, 43-71.

(10) Splendiani, A.; Sun, L.; Zhang, Y.; Li, T.; Kim, J.; Chim, C.-Y.; Galli, G.; Wang, F., Emerging Photoluminescence in Monolayer MoS_2. *Nano Lett.* **2010**, *10*, 1271-1275.

(11) Navarro-Moratalla, E.; Island, J. O.; Mañas-Valero, S.; Pinilla-Cienfuegos, E.; Castellanos-Gomez, A.; Quereda, J.; Rubio-Bollinger, G.; Chirolli, L.; Silva-Guillén, J. A.; Agraït, N.; et al., Enhanced Superconductivity in Atomically Thin TaS_2. *Nat. Commun.* **2016**, *7*, 11043.

(12) Shao, B.; Eich, A.; Sanders, C.; Ngankeu, A. S.; Bianchi, M.; Hofmann, P.; Khajetoorians, A. A.; Wehling, T. O., Pseudodoping of a Metallic Two-Dimensional Material by the Supporting Substrate. *Nat. Commun.* **2019**, *10*, 180.

(13) Stan, R.-M.; Mahatha, S. K.; Bianchi, M.; Sanders, C. E.; Curcio, D.; Hofmann, P.; Miwa, J. A., Epitaxial Single-Layer NbS_2 on Au(111): Synthesis, Structure, and Electronic Properties. *Phys. Rev. Mater.* **2019**, *3*, 044003.

(14) Li, F.; Tang, Q., Modulating the Electronic Structure and in-Plane Activity of Two-Dimensional Transition Metal Dichalcogenide (MoS_2, TaS_2, NbS_2) Monolayers by Interfacial Engineering. *J. Phys. Chem. C* **2020**, *124*, 8822-8833.

(15) Lefcochilos-Fogelquist, H. M.; Albertini, O. R.; Liu, A. Y., Substrate-Induced Suppression of Charge Density Wave Phase in Monolayer 1H-TaS_2 on Au(111). *Phys. Rev. B* **2019**, *99*, 174113.

(16) Hall, J.; Ehlen, N.; Berges, J.; van Loon, E.; van Efferen, C.; Murray, C.; Rösner, M.; Li, J.; Senkovskiy, B. V.; Hell, M.; et al., Environmental Control of Charge Density Wave Order in Monolayer 2H-TaS_2. *ACS Nano* **2019**, *13*, 10210-10220.

(17) Peng, J.; Yu, Z.; Wu, J.; Zhou, Y.; Guo, Y.; Li, Z.; Zhao, J.; Wu, C.; Xie, Y., Disorder Enhanced

Superconductivity toward TaS_2 Monolayer. *ACS Nano* **2018**, *12*, 9461-9466.

(18) Pan, J.; Guo, C.; Song, C.; Lai, X.; Li, H.; Zhao, W.; Zhang, H.; Mu, G.; Bu, K.; Lin, T.; et al., Enhanced Superconductivity in Restacked TaS_2 Nanosheets. *J. Am. Chem. Soc.* **2017**, *139*, 4623-4626.

(19) Cremonsa, D. R.; Plemmonsa, D. A.; Flannigan, D. J., Defect-Mediated Phonon Dynamics in TaS_2 and WSe_2. *Struct. Dyn.* **2017**, *4*, 044019.

(20) Zhu, C.; Chen, Y.; Liu, F.; Zheng, S.; Li, X.; Chaturvedi, A.; Zhou, J.; Fu, Q.; He, Y.; Zeng, Q.; et al., Light-Tunable 1T-TaS_2 Charge-Density-Wave Oscillators. *ACS Nano* **2018**, *12*, 11203-11210.

(21) Kinyanjui, M. K.; Bjrkman, T.; Lehnert, T.; Kster, J.; Kaiser, U., Effects of Electron Beam Generated Lattice Defects on the Periodic Lattice Distortion Structure in 1T−TaS_2 and 1T−$TaSe_2$ Thin Layers. *Phys. Rev. B* **2019**, *99*, 024101.

(22) Li, H.; Tan, Y.; Liu, P.; Guo, C.; Luo, M.; Han, J.; Lin, T.; Huang, F.; Chen, M., Atomic-Sized Pores Enhanced Electrocatalysis of TaS_2 Nanosheets for Hydrogen Evolution. *Adv. Mater.* **2016**, *28*, 8945-8949.

(23) Fujii, D.; Iwasaki, T.; Akiyama, K.; Fujisawa, Y.; Demura, S.; Sakata, H., Electronic States of Domain Structure in 1T-$TaS_{2-x}Se_x$ Observed by Stm/Sts. *J. Phys.: Conf. Ser.* **2018**, *969*, 012041.

(24) Li, H.; Tsai, C.; Koh, A. L.; Cai, L.; Contryman, A. W.; Fragapane, A. H.; Zhao, J.; Han, H. S.; Manoharan, H. C.; Abild-Pedersen, F., Activating and Optimizing MoS_2 Basal Planes for Hydrogen Evolution through the Formation of Strained Sulphur Vacancies. *Nat. Mater.* **2016**, *15*, 48-53.

(25) Voiry, D.; Yang, J.; Chhowalla, M., Recent Strategies for Improving the Catalytic Activity of 2D TMD Nanosheets toward the Hydrogen Evolution Reaction. *Adv. Mater.* **2016**, *28*, 6197-6206.

(26) Guo, Y.; Park, T.; Yi, J. W.; Henzie, J.; Kim, J.; Wang, Z.; Jiang, B.; Bando, Y.; Sugahara, Y.; Tang, J.; et al., Nanoarchitectonics for Transition-Metal-Sulfide-Based Electrocatalysts for Water Splitting. *Adv. Mater.* **2019**, *31*, 1807134.

(27) Sun, X.; Dai, J.; Guo, Y.; Wu, C.; Hu, F.; Zhao, J.; Zeng, X.; Xie, Y., Semimetallic Molybdenum Disulfide Ultrathin Nanosheets as an Efficient Electrocatalyst for Hydrogen Evolution. *Nanoscale* **2014**, *6*, 8359-8367.

(28) Tan, Y.; Liu, P.; Chen, L.; Cong, W.; Ito, Y.; Han, J.; Guo, X.; Tang, Z.; Fujita, T.; Hirata, A.; et al., Monolayer MoS_2 Films Supported by 3D Nanoporous Metals for High-Efficiency Electrocatalytic Hydrogen Production. *Adv. Mater.* **2014**, *26*, 8023-8028.

(29) Voiry, D.; Salehi, M.; Silva, R.; Fujita, T.; Chen, M.; Asefa, T.; Shenoy, V. B.; Eda, G.; Chhowalla, M., Conducting MoS_2 Nanosheets as Catalysts for Hydrogen Evolution Reaction. *Nano Lett.* **2013**, *13*, 6222-6227.

(30) Liu, Y.; Wu, J.; Hackenberg, K. P.; Zhang, J.; Wang, Y. M.; Yang, Y.; Keyshar, K.; Gu, J.; Ogitsu, T.; Vajtai, R.; et al., Self-Optimizing, Highly Surface-Active Layered Metal Dichalcogenide Catalysts for Hydrogen Evolution. *Nat. Energy* **2017**, *2*, 17127.

(31) Najafi, L.; Bellani, S.; Oropesa-Nuñez, R.; Martín-García, B.; Prato, M.; Pasquale, L.; Panda, J.-K.; Marvan, P.; Sofer, Z.; Bonaccorso, F., TaS_2, $TaSe_2$, and Their Heterogeneous Films as Catalysts for the Hydrogen Evolution Reaction. *ACS Catal.* **2020**, *10*, 3313-3325.

(32) Huan, Y.; Shi, J.; Zou, X.; Gong, Y.; Xie, C.; Yang, Z.; Zhang, Z.; Gao, Y.; Shi, Y.; Li, M.; et al., Scalable Production of Two-Dimensional Metallic Transition Metal Dichalcogenide Nanosheet Powders Using Nacl Templates toward Electrocatalytic Applications. *J. Am. Chem. Soc.* **2019**, *141*, 18694-18703.

(33) Shi, J.; Wang, X.; Zhang, S.; Xiao, L.; Huan, Y.; Gong, Y.; Zhang, Z.; Li, Y.; Zhou, X.; Hong, M.; et al., Two-Dimensional Metallic Tantalum Disulfide as a Hydrogen Evolution Catalyst. *Nat. Commun.*

2017, *8*, 958.

(34) Huan, Y.; Shi, J.; Zou, X.; Gong, Y.; Zhang, Z.; Li, M.; Zhao, L.; Xu, R.; Jiang, S.; Zhou, X.; et al., Vertical 1T-TaS_2 Synthesis on Nanoporous Gold for High-Performance Electrocatalytic Applications. *Adv. Mater.* **2018**, *30*, 1705916.

(35) Kohn, W.; Sham, L. J., Self-Consistent Equations Including Exchange and Correlation Effects. *Phys. Rev.* **1965**, *140*, A1133.

(36) Kresse, G.; J, F., Efficient Iterative Schemes for Ab Initio Total-Energy Calculations Using a Plane-Wave Basis Set. *Phys. Rev. B: Condens. Matter Mater. Phys.* **1996**, *54*, 11169-11186.

(37) Blochl, P. E., Projector Augmented-Wave Method. *Phys. Rev. B* **1994**, *50*, 17953-17979.

(38) Kresse, G.; Joubert, D., From Ultrasoft Pseudopotentials to the Projector Augmented-Wave Method. *Phys. Rev. B: Condens. Matter Mater. Phys.* **1999**, *59*, 1758-1775.

(39) Perdew, J. P.; Burke, K.; Ernzerhof, M., Generalized Gradient Approximation Made Simple. *Phys. Rev. Lett.* **1996**, *77*, 3865-3868.

(40) Grimme, S.; Antony, J.; Ehrlich, S.; Krieg, H., A Consistent and Accurate Ab Initio Parametrization of Density Functional Dispersion Correction (DFT-D) for the 94 Elements H-Pu. *J. Chem. Phys.* **2010**, *132*, 154104.

(41) Henkelman, G.; Uberuaga, B. P.; Jónsson, H., A Climbing Image Nudged Elastic Band Method for Finding Saddle Points and Minimum Energy Paths. *J. Chem. Phys.* **2000**, *113*, 9901-9904.

(42) Koch, C. Determination of Core Structure Periodicity and Point Defect Density Along Dislocations. Ph.D. Dissertation, Arizona State University, 2002.

(43) Spijkerman, A.; de Boer, J. L.; Meetsma, A.; Wiegers, G. A.; van Smaalen, S., X-Ray Crystal-Structure Refinement of the Nearly Commensurate Phase of 1*T*-TaS_2 in (3+2)-Dimensional Superspace. *Phys. Rev. B* **1997**, *56*, 13757-13767.

(44) Gao, N.; Guo, Y.; Zhou, S.; Bai, Y.; Zhao, J., Structures and Magnetic Properties of MoS_2 Grain Boundaries with Antisite Defects. *J. Phys. Chem. C* **2017**, *121*, 12261-12269.

(45) Hong, J.; Hu, Z.; Probert, M.; Li, K.; Lv, D.; Yang, X.; Gu, L.; Mao, N.; Feng, Q.; Xie, L., Exploring Atomic Defects in Molybdenum Disulphide Monolayers. *Nat. Commun.* **2015**, *6*, 6293.

(46) Miralrio, A.; Cortes, E. R.; Castro, M., Electronic Properties and Enhanced Reactivity of MoS_2 Monolayers with Substitutional Gold Atoms Embedded into Sulfur Vacancies. *Appl. Surf. Sci.* **2018**, *455*, 758-770.

(47) Haldar, S.; Vovusha, H.; Yadav, M. K.; Eriksson, O.; Sanyal, B., Systematic Study of Structural, Electronic, and Optical Properties of Atomic-Scale Defects in the Two-Dimensional Transition Metal Dichalcogenides MX_2 (M = Mo, W; X = S, Se, Te). *Phys. Rev. B* **2015**, *92*, 235408.

(48) Guo, Y.; Liu, D.; Robertson, J., Chalcogen Vacancies in Monolayer Transition Metal Dichalcogenides and Fermi Level Pinning at Contacts. *Appl. Phys. Lett.* **2015**, *106*, 173106.

(49) Zhou, W.; Zou, X.; Najmaei, S.; Liu, Z.; Shi, Y.; Kong, J.; Lou, J.; Ajayan, P. M.; Yakobson, B. I.; Idrobo, J. C., Intrinsic Structural Defects in Monolayer Molybdenum Disulfide. *Nano Lett.* **2013**, *13*, 2615-2622.

(50) Wang, S.; Lee, G. D.; Lee, S.; Yoon, E.; Warner, J. H., Detailed Atomic Reconstruction of Extended Line Defects in Monolayer MoS_2. *ACS Nano* **2016**, *10*, 5419-5430.

(51) Zande, A. M. V. D.; Huang, P. Y.; Chenet, D. A.; Berkelbach, T. C.; Hone, J. C., Grains and Grain Boundaries in Highly Crystalline Monolayer Molybdenum Disulfide. *Nat. Mater.* **2013**, *12*, 554-561.

(52) Najmaei, S.; Liu, Z.; Zhou, W.; Zou, X.; Shi, G.; Lei, S.; Yakobson, B. I.; Idrobo, J. C.; Ajayan, P. M.; Lou, J., Vapour Phase Growth and Grain Boundary Structure of Molybdenum Disulphide Atomic

Layers. *Nat. Mater.* **2013**, *12*, 754-759.

(53) Guo, Y.; Zhou, S.; Zhang, J.; Bai, Y.; Zhao, J., Atomic Structures and Electronic Properties of Phosphorene Grain Boundaries. *2D Mater.* **2016**, *3*, 025008.

(54) Becke, A. D.; Edgecombe, K. E., A Simple Measure of Electron Localization in Atomic and Molecular Systems. *J. Chem. Phys.* **1990**, *92*, 5397-5403.

(55) Guan, X.; Zhu, G.; Wei, X.; Cao, J., Tuning the Electronic Properties of Monolayer MoS_2, $MoSe_2$ and MoSSe by Applying Z-Axial Strain. *Chem. Phys. Lett.* **2019**, *730*, 191-197.

(56) Noerskov, J. K.; Bligaard, T.; Logadottir, A.; Kitchin, J. R.; Chen, J. G.; Pandelov, S.; Stimming, U., Trends in the Exchange Current for Hydrogen Evolution. *J. Electrochem. Chem.* **2005**, *152*, J23-J26.

(57) Chase, M. W., *NIST-JANAF Thermochemical Tables*, American Institute of Physics, New York 1998.

(58) Hammer, B.; Norskov, J. K., Why Gold Is the Noblest of All the Metals. *Nature* **1995**, *376*, 238-240.

(59) Ouyang, Y.; Ling, C.; Chen, Q.; Wang, Z.; Shi, L.; Wang, J., Activating Inert Basal Planes of MoS_2 for Hydrogen Evolution Reaction through the Formation of Different Intrinsic Defects. *Chem. Mater* **2016**, *28*, 4390-4396.